Two-dimensional PSF prediction of multiple-reflection optical systems with rough surfaces

Kashmira Tayabaly[1,2], Daniele Spiga[1], Giorgia Sironi[1], Giovanni Pareschi[1], Michele Lavagna[2]

[1] INAF/Brera Astronomical Observatory, Via Bianchi 46, 23807 Merate, Italy
[2] Politecnico di Milano, Via La Masa 1, 20156 Milano, Italy

ABSTRACT

The focusing accuracy in reflective optical systems, usually expressed in terms of the Point Spread Function (PSF) is chiefly determined by two factors: the deviation of the mirror shape from the nominal design and the surface finishing. While the effects of the former are usually well described by the geometrical optics, the latter is diffractive/interferential in nature and determined by a distribution of defects that cover several decades in the lateral scale (from a few millimeters to a few microns). Clearly, reducing the level of scattered light is crucial to improve the focusing of the collected radiation, particularly for astronomical telescopes that aim to detect faint light signals from our Universe. Telescopes are typically arranged in multiple reflections configuration and the behavior of the multiply-scattered radiation becomes difficult to predict and control. Also it is difficult to disentangle the effect of surface scattering from the PSF degradation caused by the shape deformation of the optical elements. This paper presents a simple and unifying method for evaluating the contribution of optical surfaces defects to the two-dimensional PSF of a multi-reflections system, regardless of the classification of a spectral range as "geometry" or "roughness". This method, entirely based on Huygens-Fresnel principle in the far-field approximation, was already applied in grazing-incidence X-ray mirrors and experimentally validated for a single reflection system, accounting for the real surface topography of the optics. In this work we show the extension of this formalism to a double reflection system and introducing real microroughness data. The formalism is applied to a MAGIC-I panel mirror that was fully characterized, allowing us to predict the PSF and the validation with real measurements of the double reflection ASTRI telescope, a prototype of CTA-SST telescope.

Keywords: PSF computation, surface metrology, physical optics, multiple reflections, surface scattering

1. INTRODUCTION

The increasing need of high-resolution imaging systems requires designing and fabricating optical systems with very tight specifications to reach the best possible optical performances. Nowadays, we can reach resolutions close to the limit of diffraction thanks to techniques like Adaptive Optics. However, high-quality instruments are usually complex systems necessary to minimize optical aberrations and to achieve the desired resolution. Increasing the number of optical elements also amplifies the light scattering, that is increasing the amount of angular spread on the detector plane that are caused by imperfections on the surface errors. As already broadly conveyed,[1–4] surface scattering properties are strongly related to the roughness structure properties and incident wavelength. The more complex the optical system, the harder it is to simulate the broadening of the focal spot caused by the scattering. Hence, to effectively control and limit the effect of surface scattering in a complex optical system, it is crucial to predict the effect of surface imperfections of all the optical surfaces onto the imaging properties of the system, particularly in terms of Point Spread Function (PSF) broadening.

Theories on surface scattering are multiple and vastly extended but no general consensus has been found so far on how to generally process surface information. To simplify and fasten computations, scattering problems are commonly treated in an analytical way as it is the case for the Beckmann-Kirchhoff theory,[2] the Rayleigh-Rice vector perturbation theory,[3] the classical Harvey-Shack scattering theory,[4] but they cannot be extended to non-stochastic surface defects such as mid-frequencies or long-period figure errors, which are typically analyzed

contact author: E-mail: kashmira.tayabaly@brera.inaf.it, Telephone: +39 02 72320428

Reflection, Scattering, and Diffraction from Surfaces V, edited by Leonard M. Hanssen, Proc. of SPIE Vol. 9961, 99610N · © 2016 SPIE · CCC code: 0277-786X/16/$18 · doi: 10.1117/12.2235410

by means of geometrical optics methods. At the same time, ray-tracing methods so widespread in predicting the PSF of optical systems cannot be used to describe the impact of surface roughness.

Setting a boundary between these two regimes is not easy; neither, is clear how one should combine the PSFs resulting from these two separate treatments. We therefore developed a general, unrestricted, and unifying formalism based on the Huygens-Fresnel principle to simulate the PSF of multiple-reflection optical systems with surfaces affected by various fabrication errors. This formalism has proved itself in multiple applied cases, either grazing-incidence mirrors where the PSF is essentially mono-dimensional[5–7] or to near-normal single mirrors in 2D geometry, always including figure errors and mid-frequencies.[8,9] In this paper, we include the microroughness contribution to the PSF degradation in the practical case of the first-generation diamond milled mirror panel[10] of MAGIC I (Major Atmospheric Gamma Imaging Cherenkov Telescopes) and we extend the 2D formalism based on physical optics to double reflection systems such as ASTRI-SST, a Schwarzschild-Couder designed prototype of the Cherenkov Telescope Array small sized telescope (CTA-SST) developed at INAF-OAB.[11]

2. SINGLE REFLECTION PSF AND APPLICATION TO MAGIC-I MIRRORS

2.1 Review of PSF computation theory

We briefly review here the formalism based on the Huygens-Fresnel principle in far-field approximation. We adopt a reference frame with the mirror profile described by the function $z_1(x_1, y_1)$, over a pupil M_1 of generic shape and size with area A_{M_1} (Fig. 1). We select the origin of the reference frame setting $z_1(0,0)=0$. The source S, located at (x_S, y_S, z_S), is assumed to be point-like and perfectly monochromatic of wavelength λ. The off-normal, average incidence angle on the mirror is θ_S. The diffracted intensity is recorded at the position $P(x_2, y_2, \bar{z_2})$, which may represent a location on either a detector array or the surface of the secondary mirror, if included in the optical layout. The detection array is parallel to the xy plane, at a constant height $\bar{z_2}$.

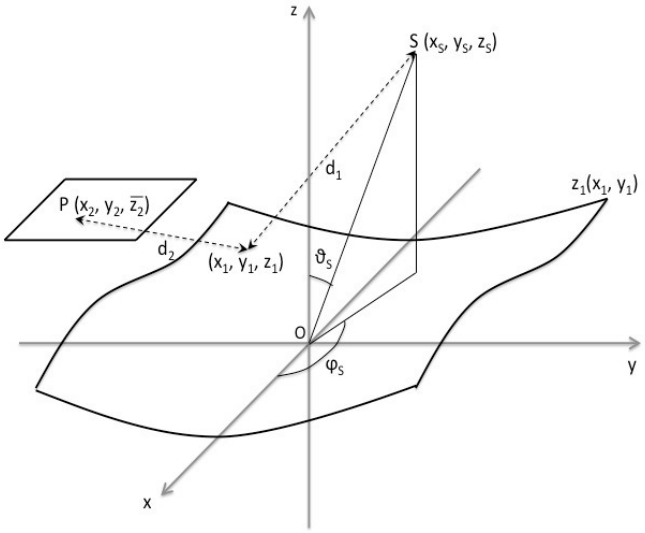

Figure 1. Scheme of computation for the electric field[8] from the source S, diffracted by a mirror described by the profile $z_1(x_1, y_1)$ at the (x_2, y_2, $\bar{z_2}$) location on the detection plane (or the secondary mirror surface). Polarization effects are neglected because in far-field conditions the elementary diffracted field vectors can be considered parallel.

We now define CPF_1, the Complex Pupil Function of the primary mirror, as:

$$\mathrm{CPF}_1(x_1, y_1) = \chi_{M_1}\, e^{\frac{4\pi \mathrm{i}}{\lambda}\Delta z_1}, \tag{1}$$

where χ_{M1} is the characteristic function of the primary mirror pupil. We define Δz_1 as

$$\Delta z_1 = z_1(x_1, y_1) - \frac{x_1^2 + y_1^2}{4z_R}, \tag{2}$$

i.e., the difference between the true mirror profile and a parabola with focal length z_{R}, where

$$\frac{1}{z_{\mathrm{R}}} = \frac{1}{z_{\mathrm{S}}} + \frac{1}{\bar{z_2}}. \tag{3}$$

Assuming that $\bar{z_2} \gg z_1$, $z_{\mathrm{S}} \gg z_1$ over the entire mirror map, that $\bar{z_2}$ and z_{S} are much larger than the mirror lateral size, and that the PSF is observed in directions near the specular one, we can easily reduce the 2D Fresnel integrals to a 2D Fourier Transform. The detailed development of the computation and the expression of the electric field at the detection plane $z = \bar{z_2}$ have been reported in previous papers.[8,9] The result, rewritten in terms of the CPF defined in Eq. 1, reads:

$$E_2(\underline{r}_2, \bar{z_2}) = \frac{E_0}{\lambda \bar{z_2}} \cos\theta_{\mathrm{S}}\, e^{-\frac{\pi \mathrm{i}}{\lambda \bar{z_2}} \|\underline{r}_2\|^2} \int \mathrm{d}^2\underline{r}_1\, \mathrm{CPF}_1(\underline{r}_1)\, e^{2\pi \mathrm{i} \underline{f}_2 \cdot \underline{r}_1}, \tag{4}$$

where we shortly denoted $\underline{r}_1 = (x_1, y_1)$, $\underline{r}_2 = (x_2, y_2)$, $\|\underline{r}_2\|^2 = x_2^2 + y_2^2$, the integration is extended to the entire $x_1 y_1$ plane, and the spatial frequencies $\underline{f}_2 = (f_{2x}, f_{2y})$ are defined by the equations:

$$f_{2x} = \frac{1}{\lambda}\left(\frac{x_2}{\bar{z_2}} + \frac{x_{\mathrm{S}}}{z_{\mathrm{S}}}\right), \qquad\qquad f_{2y} = \frac{1}{\lambda}\left(\frac{y_2}{\bar{z_2}} + \frac{y_{\mathrm{S}}}{z_{\mathrm{S}}}\right). \tag{5}$$

The specular direction of the source ($\underline{f}_2 = (0,0)$) is correctly defined as $x_2/z_2 = -x_{\mathrm{S}}/z_{\mathrm{S}}$, and $y_2/z_2 = -y_{\mathrm{S}}/z_{\mathrm{S}}$. As of now, we are only interested in the single reflection PSF, we neglect phase factors in Eq. 4 and define the Optical Transfer Function (OTF) of the primary mirror as

$$\mathrm{OTF}_1(\underline{r}_2) = \frac{1}{A_{\mathrm{M}_1}} \int \mathrm{d}^2\underline{r}_1\, \mathrm{CPF}_1(\underline{r}_1)\, e^{2\pi \mathrm{i} \underline{f}_2 \cdot \underline{r}_1}. \tag{6}$$

Computing now the radiation flux at the detection plane from Eq. 4 and normalizing to the flux impinging on the mirror,[8] we obtain the Point Spread Function (PSF) of the primary mirror as

$$\mathrm{PSF}_1(\underline{r}_2) = \frac{A_{\mathrm{M}_1}}{\lambda^2 {\bar{z_2}}^2} |\mathrm{OTF}_1(\underline{r}_2)|^2. \tag{7}$$

An alternative expression for the PSF can be obtained using the Wiener-Khintchine theorem to remove the squared module of the OTF,

$$\mathrm{PSF}_1(\underline{r}_2) = \frac{1}{\lambda^2 {\bar{z_2}}^2} \int \mathrm{d}^2\underline{h}_1\, e^{-2\pi \mathrm{i} \underline{f}_2 \cdot \underline{h}_1}\, \widetilde{\mathrm{CPF}}_1(\underline{h}_1), \tag{8}$$

having denoted with $\widetilde{\mathrm{CPF}}_1$ the autocorrelation function of the CPF_1,

$$\widetilde{\mathrm{CPF}}_1(\underline{h}_1) = \frac{1}{A_{\mathrm{M}_1}} \int \mathrm{d}^2\underline{r}_1\, \mathrm{CPF}_1(\underline{r}_1)\, \mathrm{CPF}_1^*(\underline{r}_1 + \underline{h}_1). \tag{9}$$

The factor appearing in front of Eq. 7 ensures that the integral of PSF over the secondary surface area is 1,

$$\begin{aligned} \int \mathrm{d}^2\underline{r}_2\, \mathrm{PSF}_1(\underline{r}_2) &= \int \frac{\mathrm{d}^2\underline{r}_2}{\lambda^2 {\bar{z_2}}^2} \int \mathrm{d}^2\underline{h}_1\, e^{-2\pi \mathrm{i} \underline{f}_2 \cdot \underline{h}_1} \widetilde{\mathrm{CPF}}_1(\underline{h}_1) = \int \mathrm{d}^2\underline{h}_1\, \widetilde{\mathrm{CPF}}_1(\underline{h}_1) \int \mathrm{d}^2\underline{f}_2\, e^{-2\pi \mathrm{i} \underline{f}_2 \cdot \underline{h}_1} = \\ &= \int \mathrm{d}^2\underline{h}_1\, \widetilde{\mathrm{CPF}}_1(\underline{h}_1)\, \delta(\underline{h}_1) = \widetilde{\mathrm{CPF}}_1(\underline{0}) = \frac{1}{A_{\mathrm{M}_1}} \int \mathrm{d}^2\underline{r}_1 |\mathrm{CPF}(\underline{r}_1)|^2 = \frac{1}{A_{\mathrm{M}_1}} \int \mathrm{d}^2\underline{r}_1 |\ \chi_{\mathrm{M}_1}(\underline{r}_1)|^2 = 1, \end{aligned} \tag{10}$$

regardless of the surface topography $z_1(\underline{r}_1)$, which only affects Δz_1 (Eq. 2). In the previous equation, $\delta(\underline{h}_1)$ denotes the Dirac delta function.

Performing the PSF computation, the following sampling rules should be followed to avoid aliasing issues:

- the CPF should at least be as large as $2L_1$, where L_1 is the maximum mirror size,[12]
- the CPF and the OTF should be sampled at spatial steps smaller than, respectively,[8]

$$\Delta x_1 = \frac{\lambda \bar{z_2}}{2L_2 \cos\theta_S}, \qquad \Delta x_2 = \frac{\lambda \bar{z_2}}{2L_1 \cos\theta_S}, \tag{11}$$

where L_2 is the detector size. The PSF is eventually resampled (usually down-sampled) to the pixel size.

The form of the PSF depends on the mirror topography. If $z_1(\underline{r}_1)$ is computed or measured, one just has to utilize its expression to substitute in Eq. 4 and solve the integral. However, different measurements systems are characterized by a different spatial resolution, and the true topography often result from the superposition of N maps including different ranges of spatial frequencies:[9]

$$z_1(\underline{r}_1) = \sum_{j=0}^{N} z_j(\underline{r}_1). \tag{12}$$

In our case, we decomposed z_1 into the geometrical surface topography $z_g(\underline{r}_1)$ – in turn including the theoretical shape of the mirror $z_{th}(\underline{r}_1)$ and its figure errors $z_e(\underline{r}_1)$ – and $z_r(x, y)$, the map describing the microroughness of the mirror,

$$z_1(\underline{r}_1) = z_g(\underline{r}_1) + z_r(\underline{r}_1), \tag{13}$$

having assumed that $\langle z_r \rangle = 0$. From Eq. 1 we obtain a total CPF as the product of the CPFs from the individual terms into which we decomposed the total topography:

$$\mathrm{CPF}_1(\underline{r}_1) = \chi_{M_1}(\underline{r}_1) e^{\frac{4i\pi}{\lambda}\left[z_g(\underline{r}_1) - \frac{\|\underline{r}_1\|^2}{4z_R}\right]} e^{\frac{4i\pi}{\lambda} z_r(\underline{r}_1)}, \tag{14}$$

and passing to the Fourier Transform of the CPF (Eq. 6), we have

$$\mathrm{OTF}_1 = \mathcal{F}\left(\chi_{M_1}\, e^{\frac{4\pi i}{\lambda}\Delta z_g}\right) \otimes \mathcal{F}\left(e^{\frac{4\pi i}{\lambda} z_r}\right). \tag{15}$$

The total PSF is therefore obtained taking the squared module of Eq. 15 and multiplying by the normalization factor (Eq. 7). There is some advantage in computing the separate OTFs and then convolving to retrieve the total OTF. In fact, the computation of the total CPF (Eq. 14) would require resampling z_g at the spatial resolution of the roughness map, which is usually much tighter. In contrast, the OTF convolution reduces the computation complexity, because the size of the roughness map can be tuned to the detector resolution using the second one of Eqs. 11, usually oversampling the real pixel size. The computation of the roughness OTF usually requires one to reconstruct the surface from a power spectral density (PSD) measurement[13] after increasing its spectral resolution by the ratio geometric map size / roughness map size (we see an example of this procedure in Sect. 2.2.2).

2.2 MAGIC-I: mirror roughness contribution to the telescope performances

MAGIC-I is the first unit, operational since 2004, of a system of two Imaging Atmospheric Cherenkov Telescopes (IACT) located at the *Roque de los Muchachos Observatory* on La Palma Island (Spain), detecting UV-blue light pulses[14] generated by cosmic rays traveling faster than light in the stratospheric medium. Each MAGIC telescope (Fig. 2) is a 17 m in diameter single reflection parabolic telescope with a focal length of 17 m. The 236 m^2 area of MAGIC-I primary mirror was originally tessellated into 964 square mirror panels 495 mm $\times$ 495 mm of size. Each panel is a spherical mirror with radius of curvature varying between 34 m and 36 m.[15]

Although surface roughness contribution in the detector space of surface scattering may not be negligible and could even be critical in some optical systems, real surface roughness is seldom properly taken into account in PSF computation. The MAGIC-I mirror panel under investigation in this study was exposed to environmental hazards for 10 years and refurbished. We characterized its surface over a wide range of spatial frequencies and used these data to simulate the PSF performances of the mirror, compared those simulations with real experimental PSF acquisitions for validation and extended the study further to analyze surface scattering contribution in focus and for degraded surfaces.

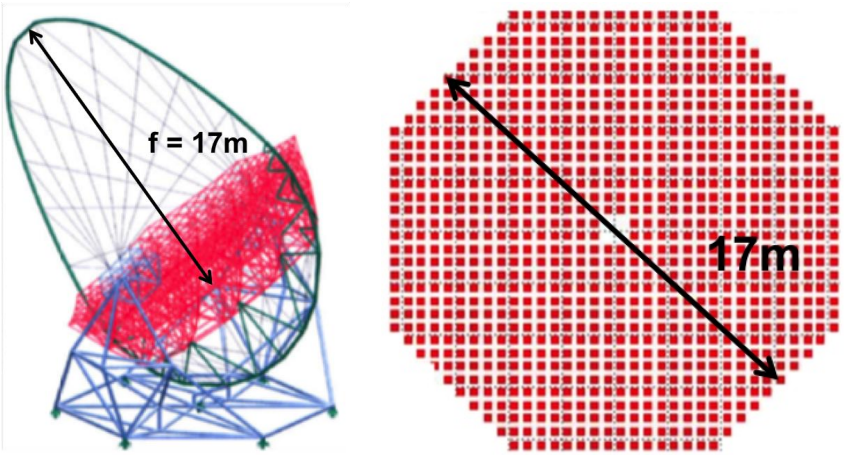

A) B)

Figure 2. Optical design of MAGIC I. A) 3D optical layout for MAGIC I telescope B) MAGIC I M1 tessellation into 964 square panels of 0.25 m^2 area (image credits: M. Doro[15]).

2.2.1 MAGIC-I mirror surface characterization

Deflectometry In order to characterize the low-frequency and part of the mid-frequency components of the mirror surface, we used the deflectometry technique, consisting of retrieving surface slope errors via distortion detection of a grid image. This is a method systematically used and perfected for Cherenkov mirror characterization at INAF-OAB: a detailed description of the experimental setup can be found in another paper.[16] Such a deflectometry experiment was performed to measure the figure errors of a different telescope mirror (ASTRI-SST panel) and validate the present physical optics methodology.[8] The deflectometry measurement on MAGIC-I mirror panel revealed the expected mirror curvature (Fig. 3A) superimposed to a texture of mid-frequency surface errors (Fig. 3B). The surface map has a 849 mm (approx. twice the mirror) size, a lateral resolution of 3 mm, and a global shape error of 3.6 μm peak-to-valley. In order to compute the PSF, the surface sampling needed to be increased to the step dictated by the first one of Eqs. 11, with $L_2 = 150$ mm, $\bar{z}_2 \approx 34$ m, $\lambda \approx 0.5$ μm, $\theta_S \approx 3$ deg, yielding $\Delta x_1 = 0.06$ mm. In practice, to shorten the computation time, at this stage we have adopted a sampling step of 0.2 mm. The resampled map therefore occupies a 4239×4239 matrix.

MFT The microroughness of the MAGIC-I mirror panel was measured using the MicroFinish Topographer (MFT),[13,17] an optical interferometer based on temporal phase shifting. The MFT was used with the 2.5× objective over a 3.8 mm × 2.9 mm area and a spatial resolution of 3.76 μm. As seen in Fig. 4A, regular grooves of approximately 50 μm minimum spacing, introduced by the diamond milling process used during the mirror manufacture,[10] are clearly visible on the surface. Such kind of features are completely absent on the surface of cold-slumped mirrors.[18,19] The MAGIC-I surface roughness therefore locally exhibits surface anisotropy to such extent that the resulting scattering becomes directional and oriented in the orthogonal direction, as already observed experimentally.[20]

Those real roughness measurements, combined with figure errors (Fig. 3A) were taken into account in the PSF computation of MAGIC-I mirror panel. To this end, the two-dimensional PSD_{2D} was computed from the different measurement maps and averaged to return the final roughness characterization of the surface (Fig. 4B).

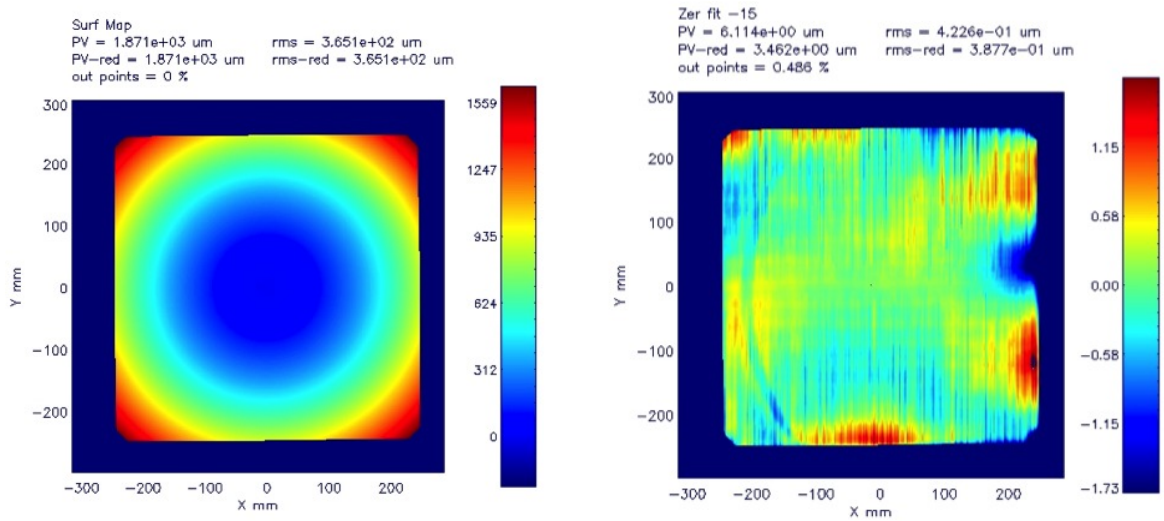

A) B)

Figure 3. MAGIC-I mirror panel: characterization of geometrical and figure error map obtained by deflectometry: A) Integrated surface map (x and y axes in millimeters, z in microns) B) Residual map after removing the first 15 Zernike polynomials to highlight the mirror defect texture.

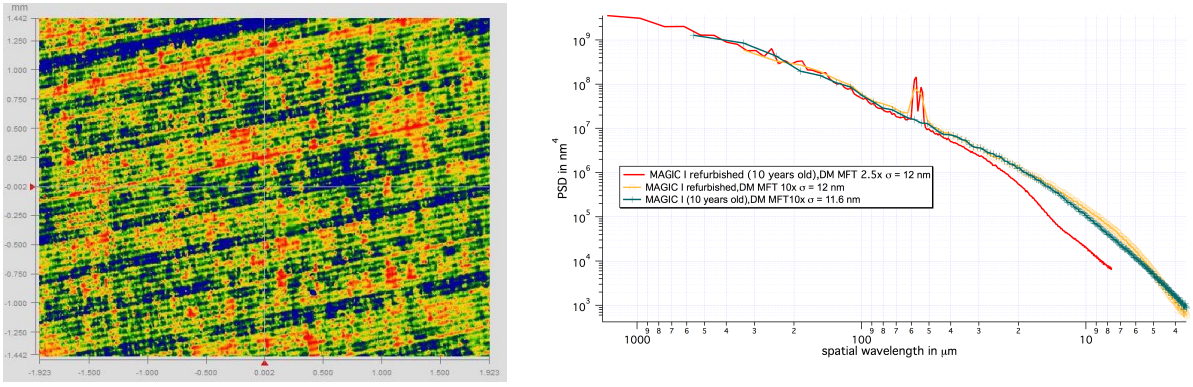

A) B)

Figure 4. A) MAGIC I roughness measurement with the MFT 2.5× objective, $\sigma = 13.4$ nm. B) PSD_{2D} azimuthally averaged vs. wavelength for MAGIC-I's mirrors measured with the MFT 2.5× and 10× objectives

2.2.2 Surface reconstruction from the PSD

As detailed in the previous sections, the optical surface roughness was measured within a mm^2 area with a lateral resolution of a few microns. We have now to extend the roughness map to the entire mirror surface of $L_x \times L_y$ sizes, and this can be done starting from the Power Spectral Density characterization derived from the MFT measurements. Assuming the PSD measurement to be representative of the roughness power spectrum throughout the entire surface, we need to extend the roughness map from a $L_x^{\rm r} \times L_y^{\rm r}$ size to the full mirror size $L_x^{\rm g} \times L_y^{\rm g}$. The surfaces are sampled with resolutions of $\Delta_x^{\rm g}$, $\Delta_y^{\rm g}$ over the geometrical map, and $\Delta_x^{\rm r}$, $\Delta_y^{\rm r}$ over the roughness map. We have $\Delta_x^{\rm g} \gg \Delta_x^{\rm r}$ and similarly for y. In the spatial frequency space, the frequency resolutions of these maps are $\Delta f_x^{\rm g} = 1/L_x^{\rm g}$, $\Delta f_x^{\rm r} = 1/L_x^{\rm r}$, and similarly for the y-axis.

The geometric map had been resampled to a resolution of $\Delta_x^{\rm g} = \Delta_y^{\rm g} = 0.2$ mm (Sect. 2.2.1); the $\mathrm{PSD_{2D}}$ of the roughness measured with the MFT was therefore trimmed in order to limit the minimum wavelength to $(\Delta_x^{\rm g}, \Delta_y^{\rm g})$, i.e. compliant with the $(\Delta_x^{\rm g}, \Delta_y^{\rm g})$ surface sampling. After trimming the high-frequency part, the integral of the PSD core includes more than 80% of the roughness rms detected with the MFT. We increased the frequency resolution of the PSD to match the frequency resolution of the geometrical map $\Delta f_x^{\rm g}, \Delta f_y^{\rm g}$ that is about 100 times tighter.

We finally reconstructed the Fourier Transform of the new surface roughness (Eq. 16). As the $\mathrm{PSD_{2D}}$ is used to report the statistically representative characterization of the surface roughness amplitudes, the phase term $\Phi(f_x^{\rm g}, f_y^{\rm g})$ information has been canceled. The phase of the different components was therefore set as random map taking values in the $[0;\, 2\pi)$ interval, and the Fourier Transform can be computed as

$$\mathcal{F}(z_1^{\rm r}) = \sqrt{\frac{\mathrm{PSD_{2D}}(f_x^{\rm g}, f_y^{\rm g})}{A_{\rm M_1}}}\, e^{i\Phi(f_x^{\rm g}, f_y^{\rm g})}. \tag{16}$$

We note that this solution is only one of the *infinitely* possible phase distributions, and that the result will not resemble the original topography in general. However, in the smooth-surface approximation – as in this case – the scattering effects are proportional solely to the PSD amplitude.[6] Under the smooth-surface approximation, the real surface phase term information is therefore irrelevant for reconstructing a roughness map that allows us to compute the scattering impact on the PSF. The problem of preserving the original phase distribution in the more general case of a rough surface will be faced in a subsequent paper. Starting from Eq. 16, an inverse Fourier Transform is used to reconstruct the surface roughness topography $z_1^{\rm r}$, extended to the full mirror area.

2.2.3 Simulation vs. Experiment

After characterizing the MAGIC-I mirror panel surface, we could simulate the PSF of MAGIC-I in intra-focal configuration (from now on denoted as pseudo-PSF), accounting for deflectometry and microroughness data. We compared the simulations with real pseudo-PSF experimental data of this same MAGIC-I panel, directly measured using the outdoor characterization facility at INAF-OAB.[21] The facility is equipped with an optical bench that allows motion in x, y and z direction for aligning the mirror to the CCD camera ProLine PL 4301E positioned tens of meters away. The mirror under test is illuminated with a blue LED light source (peaking at $\lambda = 480$ nm) in a quasi-$2f$ configuration setup. The mirror was oriented at $\theta_{\rm S} = 2.83$ deg in the yz plane and $\phi_{\rm S} = 0.86$ deg in the xz plane. Figure 5 shows the layout of the experimental setup used for MAGIC-I panel's pseudo-PSF acquisition. Despite the long optical bench setup available, the long radius of curvature of the mirror did not allow us to acquire the PSF in focus but slightly intra-focus (see Fig. 6) at the bench travel end. The MAGIC-I panel pseudo-PSF was acquired using the mosaic mode of the camera, i.e., filling a 3×3 matrix over a 150 mm × 150 mm area to recover the full image (50 mm × 50 mm) with an exposure time of 0.15 s. Very satisfying results are obtained when comparing the simulation to the real experimental acquisition, as displayed in Fig. 7.

2.2.4 Extending the simulation to focus

An in-focus PSF measurement is not always possible as it requires a dedicated setup spanning over tens of meters. In contrast, the PSF simulation is extremely flexible and easy to perform, at any light wavelength and regardless of the mirror geometry, in-focus or out-of-focus. In addition, it has the ability to assess the

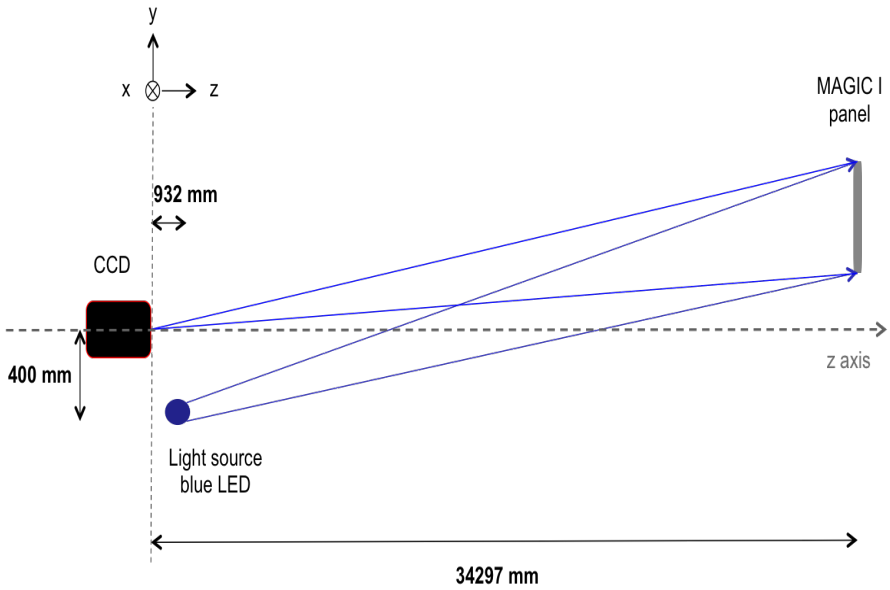

Figure 5. MAGIC-I square panel PSF acquisition setup in the outdoor optical bench at INAF-OAB.

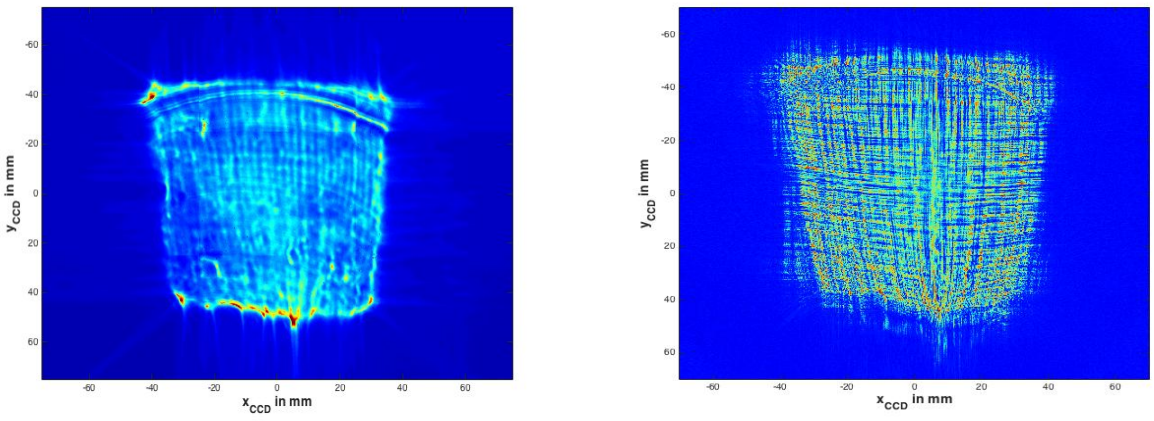

A) B)

Figure 6. MAGIC-I panel pseudo-PSF in the configuration described in Fig. 5. A) Experimental PSF acquisition in mosaic mode in the outdoor facility. B) Physical optics PSF simulation, accounting for figure errors and surface microroughness (Sect. 2.2.1), obtained applying Eq. 7.

roughness contribution to the PSF degradation. For instance, in the previous section we could only measure the pseudo-PSF in intra-focal position. Since the simulation was validated by the measurement (Sect. 2.2.3), using the physical optics simulation we can simulate the PSF in focus with the setup configuration described in Fig. 5. In other words, we simulated what we would have observed if the camera could have been placed in the mirror focus. The grooves introduced by the diamond milling process seen in Fig. 4 cause a grating effect that extend the PSF in the orthogonal direction as shown in the in-focus simulation (see Fig. 8B). The effect is enhanced when the roughness rms is supposed to be 3 times and 10 times higher (see Figs. 8C and 8D). As the low- and mid-frequency defects on the mirror prevail over microroughness, the latter's contribution is hardly visible out of focus (Fig. 6), while it starts to become visible in focus (Fig. 8B).

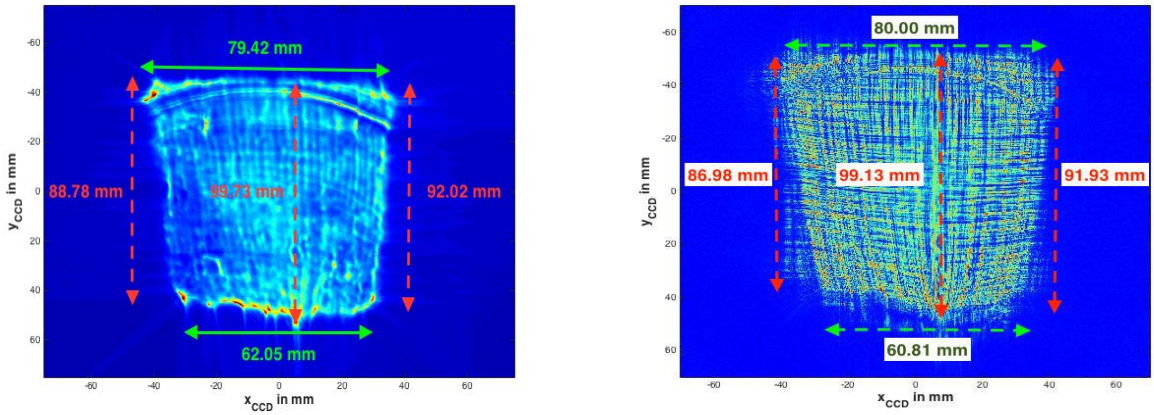

A) B)

Figure 7. The same as in Fig. 6, with size measurements. A) Experimental exposure. B) Physical optics simulation.

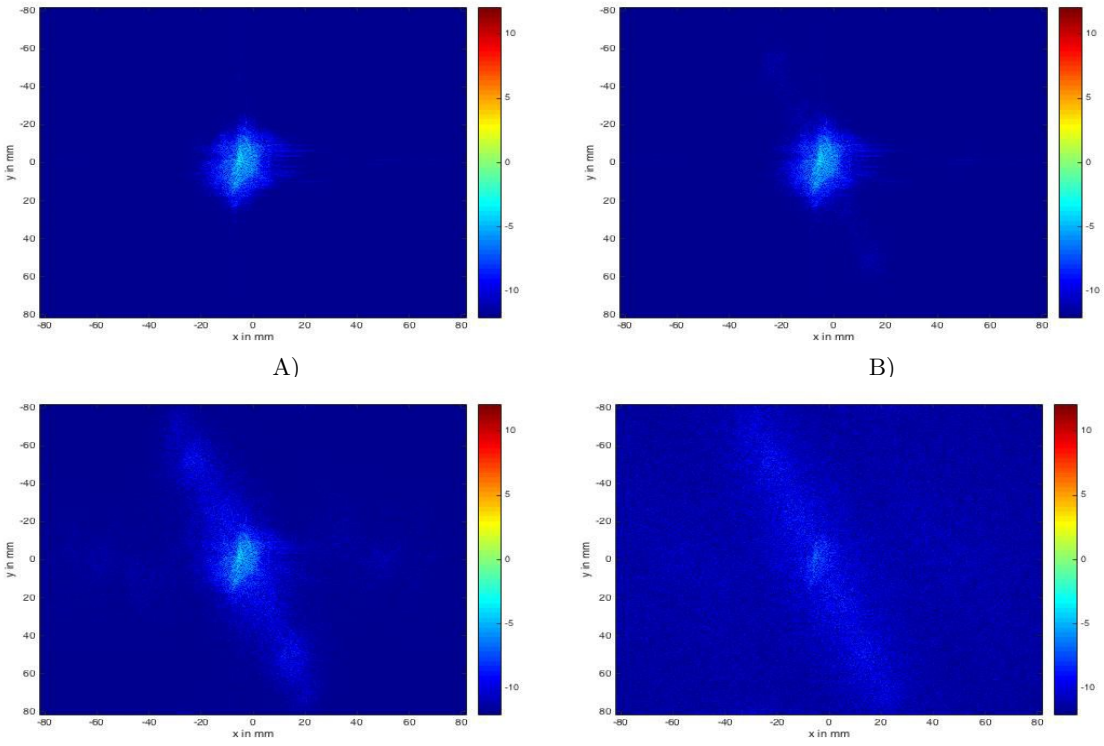

A) B)

C) D)

Figure 8. The predicted PSF MAGIC-I panel, accounting for: A) only figure errors measured by deflectometry, B) figure errors and measured surface roughness, C) figure errors and surface roughness three times higher in terms of rms, and D) figure errors and surface roughness ten times higher in terms of rms. We assumed a radius of curvature $R_c = 37.25$ m, a source set at 33.36 m from the mirror, while the detector is set in the image plane, 42.17 m from the mirror.

3. PSF COMPUTATION IN DOUBLE REFLECTION

3.1 Double reflection theory

Accounting for a second reflection essentially consists in propagating the wavefront from the secondary mirror surface M_2, described by the function $z_2(\underline{r}_2)$, to the detector plane (Fig. 9), mapped by the coordinates $\underline{r}_D = (x_D, y_D)$, at fixed height $z = z_D < \bar{z}_2$. Just like we did for the first diffraction, we still assume the reference plane

of the secondary mirror to be parallel to the xy plane and that $\langle z_2(\underline{r}_2)\rangle = \bar{z_2}$. We note that small possible tilt angles of M_2 can be included in the z_2 definition. Near the specular direction, the electric field at the reference plane is provided by Eq. 4:

$$E_2(\underline{r}_2, \bar{z_2}) = E_0 \frac{A_{M_1} \cos\theta_S}{\lambda \bar{z_2}} \, e^{-\frac{\pi i}{\lambda \bar{z_2}} \|\underline{r}_2\|^2} \, \mathrm{OTF}_1(\underline{r}_2). \tag{17}$$

where we used the OTF definition (Eq. 6). Assuming that the secondary mirror curvature is not too pronounced and that we are near normal incidence, it is reasonable to consider its amplitude as unchanged at the mirror surface with respect to the reference plane. The phase, however, will be delayed by

$$\Delta\phi_2 = \frac{2\pi \left[z_2(\underline{r}_2) - \bar{z_2}\right]}{\lambda \cos\theta_S}, \tag{18}$$

where the incidence angle on the secondary mirror has been considered constant throughout the secondary mirror surface M_2.

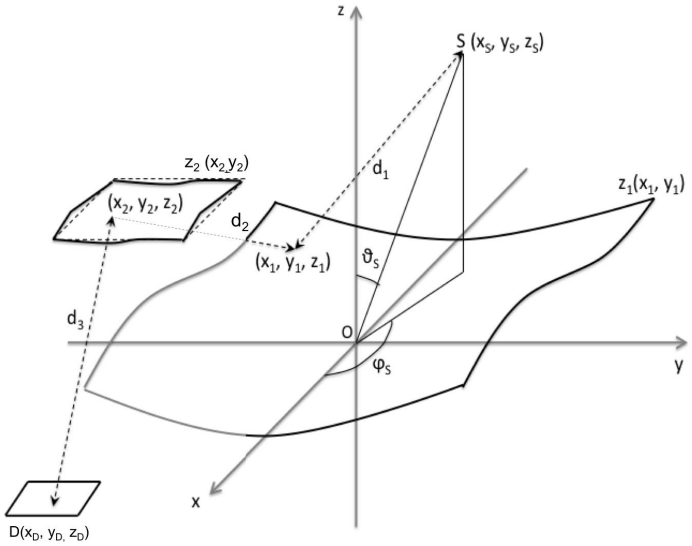

Figure 9. Scheme of computation for the electric field diffracted twice by a primary and a secondary mirror described by the profile $z_2(\underline{r}_2)$ at the (x_D, y_D, z_D) location on the detection plane. The area with dashed contour is the reference plane at $z = \bar{z_2}$ used to compute E_2. Also in this case we neglect polarization effects.

The subsequent near-normal diffraction is simply accounted for by propagating the electric field to the detector plane at $z = z_D$:

$$E(\underline{r}_D, z_D) = \frac{1}{\lambda |z_D - \bar{z_2}|} \int_{M_2} \mathrm{d}^2\underline{r}_2 \, E_2(\underline{r}_2, \bar{z_2}) \, e^{-i\Delta\phi_2} \, e^{-\frac{2\pi i}{\lambda} d_3}, \tag{19}$$

where E_2 is provided by Eq. 17, $\Delta\phi_2$ by Eq. 18, and

$$d_3 = \sqrt{(x_2 - x_D)^2 + (y_2 - y_D)^2 + (z_2 - z_D)^2} \approx (z_2 - z_D) + \frac{(x_2 - x_D)^2 + (y_2 - y_D)^2}{2(\bar{z_2} - z_D)}. \tag{20}$$

We were allowed to make the last passage in the far-field condition. Replacing the definition of d_3 into Eq. 19, neglecting constant phase factors, and defining the positive constant $z_{2D} = \bar{z_2} - z_D$ we get

$$E(\underline{r}_D, z_D) = E_0 \frac{A_{M_1} \cos\theta_S}{\lambda^2 \bar{z_2} z_{2D}} \, e^{-\frac{i\pi \|\underline{r}_D\|^2}{\lambda z_{2D}}} \int \mathrm{d}^2\underline{r}_2 \, \mathrm{OTF}_1(\underline{r}_2) \, e^{-\frac{4\pi i}{\lambda} \Delta z_2} \, e^{2\pi i \underline{f}_D \cdot \underline{r}_2}, \tag{21}$$

where we defined the quantity

$$\Delta z_2 = z_2 + \frac{\|\underline{r}_2\|^2}{4z_{2\mathrm{R}}}, \tag{22}$$

in which the secondary mirror topography $z_2(\underline{r}_2)$ is compared to a parabolic, concave downwards, surface with equivalent focal length

$$\frac{1}{z_{2R}} = \frac{1}{\bar{z_2}} + \frac{1}{z_{2D}}, \tag{23}$$

and the spatial frequencies are now defined as

$$\underline{f}_D = \left(\frac{x_\mathrm{D}}{\lambda z_{2\mathrm{D}}}, \frac{y_\mathrm{D}}{\lambda z_{2\mathrm{D}}} \right). \tag{24}$$

We also note that in the Δz_2 definition (Eq. 22) we have approximated $1/\cos\theta_\mathrm{S} \approx 1$ in near-normal incidence; the correction is on the order of the obliquity factor, already neglected in the single-reflection computation.[8]

Taking the square module of Eq. 21 and normalizing to the power impinging on the primary mirror, $E_0^2 \cos^2\theta_\mathrm{S} A_{\mathrm{M}_1}$ we obtain the general expression of the double reflection PSF:

$$\mathrm{PSF}_2(\underline{r}_\mathrm{D}) = \frac{A_{\mathrm{M}_1}}{\lambda^4 \bar{z_2}^2 z_{2D}^2} \left| \int \mathrm{d}^2\underline{r}_2 \, \mathrm{OTF}_1(\underline{r}_2) \, \chi_{\mathrm{M}_2}(\underline{r}_2) \, e^{-\frac{4\pi\mathrm{i}}{\lambda}\Delta z_2} \, e^{2\pi\mathrm{i}\underline{f}_\mathrm{D}\cdot\underline{r}_2} \right|^2, \tag{25}$$

where we have added another χ_{M_2} function to account for the real size of the secondary mirror – as it might in principle be smaller than $\mathrm{OTF}_1(\underline{r}_2)$. We can also introduce the $\mathrm{OTF}_2(\underline{r}_\mathrm{D})$ function,

$$\mathrm{OTF}_2(\underline{r}_\mathrm{D}) = \frac{1}{A_{\mathrm{M}_2}} \int \mathrm{d}^2\underline{r}_2 \, \mathrm{OTF}_1(\underline{r}_2) \, \mathrm{CPF}_2(\underline{r}_2) \, e^{2\pi\mathrm{i}\underline{f}_\mathrm{D}\cdot\underline{r}_2}, \tag{26}$$

having defined the complex pupil function of the secondary mirror

$$\mathrm{CPF}_2(\underline{r}_2) = \chi_{\mathrm{M}_2}(\underline{r}_2) \, e^{-\frac{4\pi\mathrm{i}}{\lambda}\Delta z_2}, \tag{27}$$

and the double reflection PSF_2 takes the compact form:

$$\mathrm{PSF}_2(\underline{r}_\mathrm{D}) = \frac{A_{\mathrm{M}_1} A_{\mathrm{M}_2}^2}{\lambda^4 \bar{z_2}^2 z_{2D}^2} \left| \mathrm{OTF}_2(\underline{r}_\mathrm{D}) \right|^2. \tag{28}$$

As we did in Sect. 2.1, we can write Eq. 28 in an alternative form,

$$\mathrm{PSF}_2(\underline{r}_\mathrm{D}) = \frac{A_{\mathrm{M}_1} A_{\mathrm{M}_2}}{\lambda^4 \bar{z_2}^2 z_{2D}^2} \int \mathrm{d}^2\underline{h}_2 \, e^{-2\pi\mathrm{i}\underline{f}_\mathrm{D}\cdot\underline{h}_2} \, \widetilde{\mathrm{OTF_1CPF}}_2(\underline{h}_2), \tag{29}$$

having denoted with $\widetilde{\mathrm{OTF_1CPF}}_2$ the autocorrelation function of the product $\mathrm{OTF}_1\mathrm{CPF}_2$. Following passages similar to the ones in Eq. 10, this expression can be used to show that also the PSF_2 is normalized to 1, provided that the OTF_1 is entirely included in the M_2 area:

$$\begin{aligned} \int \mathrm{d}^2\underline{r}_\mathrm{D} \, \mathrm{PSF}_2(\underline{r}_\mathrm{D}) = \frac{A_{\mathrm{M}_1} A_{\mathrm{M}_2}}{\lambda^2 \bar{z_2}^2} \widetilde{\mathrm{OTF_1CPF}}_2(\underline{0}) = \frac{A_{\mathrm{M}_1}}{\lambda^2 \bar{z_2}^2} \int \mathrm{d}^2\underline{r}_2 \, |\mathrm{OTF}_1(\underline{r}_2)|^2 |\mathrm{CPF}_2(\underline{r}_2)|^2 = \\ = \frac{A_{\mathrm{M}_1}}{\lambda^2 \bar{z_2}^2} \int \mathrm{d}^2\underline{r}_2 \, |\mathrm{OTF}_1(\underline{r}_2)|^2 |\chi_{\mathrm{M}_2}(\underline{r}_2)|^2 = \frac{A_{\mathrm{M}_1}}{\lambda^2 \bar{z_2}^2} \int \mathrm{d}^2\underline{r}_2 \, |\mathrm{OTF}_1(\underline{r}_2)|^2 = \int \mathrm{d}^2\underline{r}_2 \, \mathrm{PSF}_1(\underline{r}_2) = 1 \end{aligned} \tag{30}$$

where we have made use of Eq. 10 to write the last passage.

3.2 ASTRI-SST case study

The double reflection formalism developed in the previous sections was applied to one of the ASTRI (Astrofisica con Specchi a Tecnologia Replicante Italiana) mirror panels. ASTRI (Fig. 10A) is a prototype for CTA-Small Size Telescope that was fully developed at INAF-OAB.[11] Its optical design is based on a Schwarzschild-Couder configuration with a 0.5 f-number and an equivalent focal length of 2150 mm.

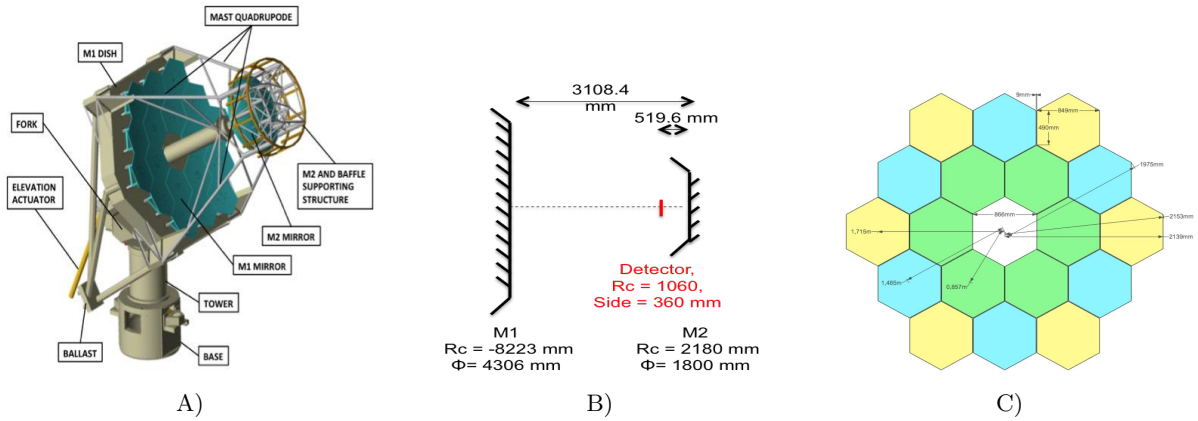

Figure 10. Optical design of ASTRI-SST. A) 3D optical layout for ASTRI-SST telescope. B) Optical design of ASTRI-SST. C) ASTRI-SST M1 design. Images after[11]

3.2.1 Theoretical shape

The ASTRI primary mirror (M1) is 4.02 m in diameter with a radius of curvature of -8223 mm, tessellated into hexagonal mirrors which face-to-face dimension is 849 mm with a 9 mm gaps in between (Fig. 10C). The M1 mirror is divided into 3 sections or 3 coronae, according to the distance of the center of the segment to the center of M1 (Fig. 10C). Therefore, the closest segments (857 mm from the center of M1) belong to corona 1 (in green in Fig. 10C), mirrors placed 1485 mm from the center of M1 are in corona 2 (in blue in Fig. 10C), and the farthest segments (1715 mm from the center of M1) are in corona 3 (in yellow in Fig. 10C).

The secondary mirror is a monolithic thick glass shell 1800 mm in diameter, with a 2180 mm radius of curvature. It is coated with a highly reflective metallic coating based on pure Aluminium and an extra protective coating of 100 nm of Quartz. Both M1 and M2 mirrors are aspherical mirrors which coefficients of asphericity are detailed in Tab. 1.

i	M1	M2
1	0	0
2	9.61060×10^{-13}	1.62076×10^{-11}
3	-5.65501×10^{-20}	-2.89584×10^{-17}
4	6.77984×10^{-27}	8.63372×10^{-24}
5	3.89558×10^{-33}	3.34856×10^{-30}
6	5.28038×10^{-40}	-1.03361×10^{-36}
7	-2.99107×10^{-47}	-6.73524×10^{-43}
8	-4.39153×10^{-53}	-3.06547×10^{-49}
9	-6.17433×10^{-60}	3.17161×10^{-55}
10	2.73586×10^{-66}	-3.71183×10^{-62}

Table 1. Coefficients of asphericity for ASTRI-SST M1 and ASTRI-SST M2.

3.2.2 Double reflection system simulation accounting for surface imperfections

Following the formalism developed in Sect. 3.1, we could extend the wave propagation into the detector space of ASTRI telescope. The simulation results for perfect M1 and M2 mirrors are displayed in Fig. 11 where we have assumed an incoming wavelength of 100 μm to reduce the computation time. As expected, we clearly detect the focal spot concentrated in a 6mm $\times$ 6mm window with diffraction fringes caused by aperture diffraction. Here the diffraction effect is enhanced by the large value of λ used for the simulation.

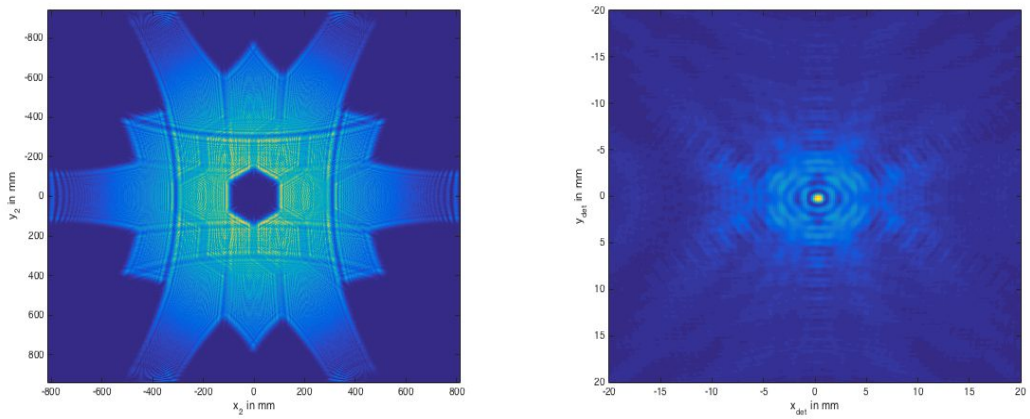

A) B)

Figure 11. Simulated image of a source on axis located 10 km (a typical height of Cherenkov flashes) away from the ASTRI-M1 fully illuminating the pupil at a wavelength of 100 μm. A) Reflection from ASTRI-M1 in the plane of ASTRI secondary mirror M2. B) 2^{nd} reflection from ASTRI-M2 in the detector plane.

As a step forward, the M1 mirror panels have been characterized using the deflectometry technique developed in[16] that reveals low spatial frequency errors, i.e., figure errors. In particular, the retrieved maps of ASTRI-COR3 panel from the slope error measurement setup is shown in Fig. 12A. The full mirror was not reconstructed as the discontinuities of the pupil made it difficult to properly retrieve the slope at the edges. Therefore, the retrieved pupil obtained by deflectometry was 822 mm $\times$ 966 mm instead of 849 mm $\times$ 980 mm, the size of the full mirror in the x and the y direction respectively. The first 500 Zernike terms were removed from the absolute surface mirror of ASTRI-COR3 in order to clearly reveal surface defects and particularly "the grid shape" error on the full panel area (0.63 m^2, Fig. 12B)). They are believed to be introduced by the Aluminum honeycomb structure put in between two thin layers of glass coated with Aluminum and Quartz (Al+SiO_2) to ensure a lightweight mirror panel.

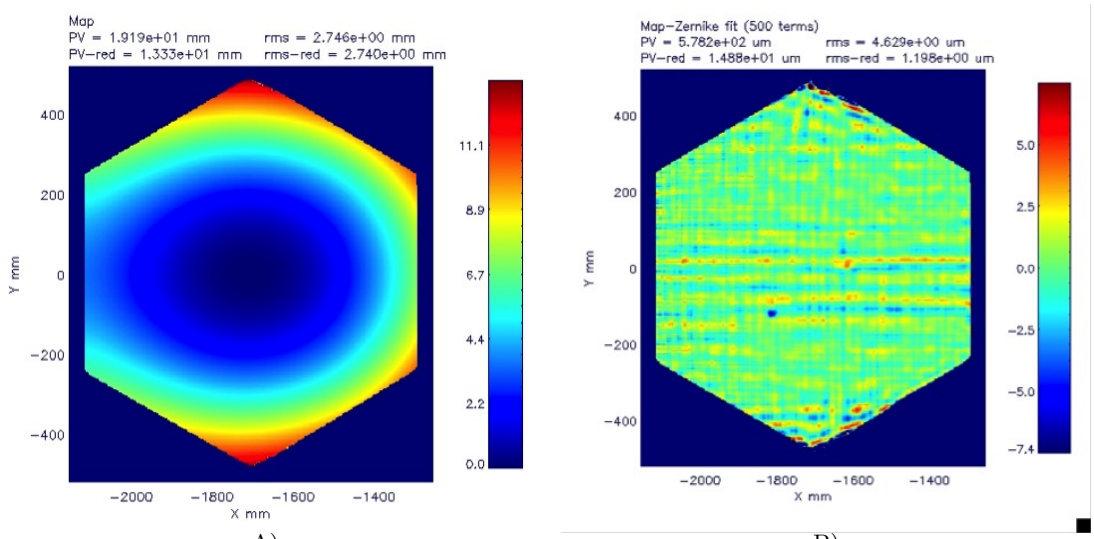

A) B)

Figure 12. Characterization of geometrical and figure error map obtained by deflectometry for ASTRI-COR3 panel: A) Measured surface topography B) surface residual errors map measurement panel after removing the first 500 Zernike polynomials

Using the ASTRI M1-COR3 surface characterization, we assumed that this segment figure errors is identical to the ones of the 17 other M1 hexagonal segments. Similarly to the previous double reflection simulation for perfect mirrors (Fig. 11), we have simulated the effect of figure errors for ASTRI-SST in the full double reflection configuration, assuming a perfect M2 with a 100 μm wavelength light source. This is obviously not the real wavelength source, but this choice does not affect the size of the reflected pattern. However, as the formalism developed and presented in this paper accounts for diffraction effects, diffraction fringes clearly appear and their spacing is enhanced on the simulated PSFs. As shown in Fig. 13 and expected, the surface defects of ASTRI-SST M1 introduce perturbation effects in the final PSF.

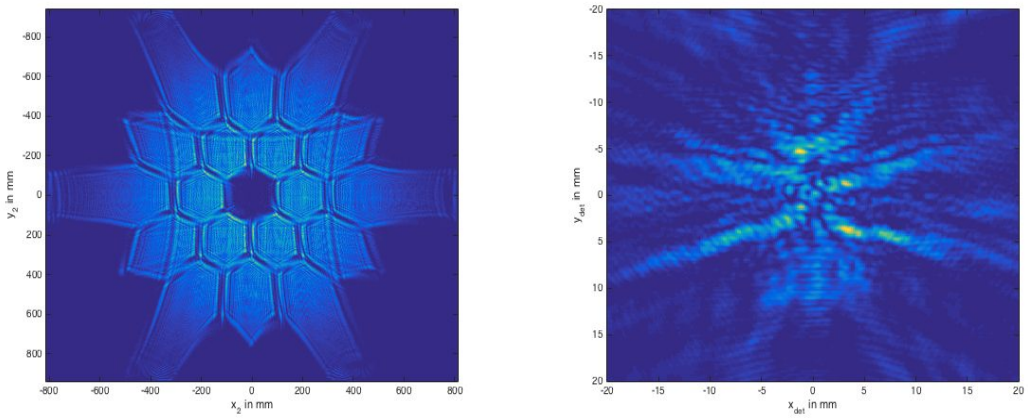

A) B)

Figure 13. Simulated image of a source on axis located 10 km away from the ASTRI-M1 fully illuminating the pupil at a wavelength of 100 μm for accounting for M1 figure errors A) Reflection from ASTRI-M1 in the plane of ASTRI secondary mirror M2. B) 2^{nd} reflection from ASTRI-M2 in the plane of the detector.

4. CONCLUSIONS

The formalism for PSF prediction presented in this paper provides a PSF computation tool for surface scattering analysis based on Huygens-Fresnel principle in the far-field approximation that is generalized and unrestricted to specific spatial frequencies regime. It allows us accounting for real and directly measured surface roughness into the PSF computation. The validity of the computation was confirmed experimentally in the case of MAGIC-I mirror panel, and the simulation was extended to roughness contribution study in-focus. The validated PSF prediction formalism has then been extended to double reflection system taking as a case study the ASTRI-SST, a Schwarzchild-Couder telescope with aspherical mirrors. The PSF simulation in focus accounted for imperfect surfaces for the hexagonal segments forming the entrance pupil of the telescope. Future work will be devoted to simulations of the PSF for CTA mirrors at the wavelength of operation in order to assess fabrication error tolerances.

ACKNOWLEDGMENTS

This work is supported by the Politecnico di Milano and the Italian National Institute for Astrophysics (INAF). A grateful acknowlegdment to Dr Giacomo Bonnoli and Dr Rodolfo Canestrari for their help and for providing key information for completing this paper.

REFERENCES

[1] Church, E.L., Jenkinson, H. A., Zavada, J.M., "Relationship between Surface Scattering and Microtopographic Features," Opt. Eng. 18(2), 182125 (1979)

[2] Beckmann, P., Spizzichino, A., "The Scattering of Electromagnetic Waves from Rough Surfaces," Pergamon Press (1963)

[3] Rice, S.O., "Reflection of electromagnetic waves from slightly rough surfaces," Commun. Pure Appl. Math. 4(2-3), 351 (1951)

[4] Harvey, J.E., "Light scattering characteristics of optical surfaces," Ph.D. Dissertation, University of Arizona (1976)

[5] Spiga, D., Raimondi, L., Furuzawa, A., Basso, S., et al., "Angular resolution measurements at SPring-8 of a hard x-ray optic for the New Hard X-ray Mission," Proc. SPIE 8147, 81470A (2011)

[6] Spiga, D., Raimondi, L., "X-ray optical systems: from metrology to Point Spread Function," Proc. SPIE 9209, 92090E (2014)

[7] Raimondi, L., Spiga, D., "Mirrors for X-ray telescopes: Fresnel diffraction-based computation of Point Spread Functions from metrology," A&A 573, A12 (2015)

[8] Tayabaly, K., Spiga, D., Sironi, G., Canestrari, R., Pareschi, G., Lavagna, M., "Computation and validation of two-dimensional PSF simulation based on physical optics," Proc. SPIE 9577, 957709 (2015)

[9] Tayabaly, K., Spiga, D., Sironi, G., Canestrari, R., Pareschi, G., Lavagna, M., "Point Spread Function computation in normal incidence for rough optical surfaces" Proc. SPIE 9911, 99111X (2016)

[10] Bastieri, D., Agguiaro, D., Arnold, J., Bigongiari, C., et al., "The Mirrors for the MAGIC Telescopes," 29th International Cosmic Ray Conference 5, 283 (2005)

[11] Pareschi, G., Agnetta, G., Antonelli, L.A., Bastieri, D., et al., "The dual-mirror Small Size Telescope for the Cherenkov Telescope Array," Proc. 33rd ICRC (2013)

[12] Spiga, D., Christensen, F.E., Bavdaz, M., Civitani, M.M., et al., "Simulation and modeling of silicon pore optics for the ATHENA x-ray telescope," Proc. SPIE 9905, 99055O (2016)

[13] Parks, R.E., "MicroFinish Topographer: surface finish metrology for large and small optics," Proc. SPIE 8126, 81260D (2011)

[14] Frank, I.M., Tamm, I.E., "Coherent visible radiation of fast electrons passing through matter," Doklady Akademii Nauk SSSR 14, 109 (1937)

[15] Doro, M., Bastieri, D., Biland, A, Dazzi, F., et al., "The reflective surface of the MAGIC telescope," NIM-A 595, 200 (2008)

[16] Sironi, G., Canestrari, R., Pareschi, G., "Deflectometry for optics evaluation: Freeform segments of polynomial mirror," Proc. SPIE 9151, 91510T (2014)

[17] Tayabaly, K., Stover, J.C., Parks, R.E., Dubin, M., Burge, J.H., "Use of the surface PSD and incident angle adjustments to investigate near specular scatter from smooth surfaces," Proc. SPIE 8838, 883805 (2013)

[18] Tayabaly, K. , Spiga, D. , Canestrari, R. , Bonnoli, G., et al., "Roughness tolerances for Cherenkov telescope mirrors," Proc. SPIE 9603, 960307 (2015)

[19] Canestrari, R., Pareschi G., Parodi F., Martelli F., Missaglia N., Banham R., "Cold shaping of thin glass foils as a method for mirror processing: from basic concepts to mass production of mirrors," Opt. Eng. 52(5), 051204 (2013)

[20] Schultz, C., "Novel All-Aluminium Mirrors of the MAGIC Telescope Project and Low Light Level Silicon Photo-Multiplier Sensors for Future Telescopes," diploma thesis (2008)

[21] Canestrari R., et al., "A facility to evaluate the focusing performance of mirrors for Cherenkov Telescopes", NIM-A 806, 61 (2015)